International Journal of Fatigue 206 (2026) 109455

Contents lists available at ScienceDirect

International Journal of Fatigue

journal homepage: www.elsevier.com/locate/ijfatigue

Defect-sensitive fatigue assessment of heavy-section ductile cast irons: a comparative study of pearlitic and high-silicon ferritic grades

M. Benedetti [a], M. Pedranz [a,b], D. Lusuardi [b], F. Zanini [c], S. Carmignato [c], V. Fontanari [a,*]

[a] Department of Industrial Engineering, University of Trento, Via Sommarive 9, Trento, Italy
[b] Fonderie Ariotti S.p.A., Adro, Italy
[c] Department of Management and Engineering, University of Padova, Stradella S. Nicola 3, Vicenza, Italy

ARTICLE INFO

Keywords:
Ductile cast iron
Uniaxial fatigue
Shrinkage pores
Highly stressed volume
Notch-pores interaction

ABSTRACT

Heavy-section castings of ductile cast iron (DCI) unavoidably contain micro shrinkage porosity due to non-uniform, slow cooling, and service components also feature geometric stress raisers. This study quantifies how these two realities—intrinsic defects and notches—jointly control fatigue resistance and formalizes a design approach that accounts for their interaction. We compare a pearlitic EN-GJS-600–3 (GJS-600–3) and a high-silicon solid solution strengthened ferritic (HSi) DCI, which exhibit different matrix ductility and distinct pore populations. Pore size distributions are characterized (via X-ray computed tomography, CT), and extreme-value statistics are used to estimate the most critical defect expected in the highly stressed region of notched specimens. This defect measure is then coupled to a strain energy density (SED) criterion to predict fatigue limits. Fatigue tests on plain and V-notched specimens with varying notch severity reveal a systematic transition from pore-dominated initiation (plain and mildly notched) to notch-dominated initiation (severe notches). The proposed CT–statistics–SED framework reproduces both the fatigue limits and the observed switch in the governing initiation site. Compared with GJS-600–3, the HSi grade shows lower intrinsic fatigue strength but greater tolerance to distributed microporosity, leading to improved reliability in geometries with large highly stressed volumes. The approach provides a practical route to defect-aware fatigue design of DCI components, suggesting material-and-geometry selection: pearlitic grades for smaller, sharper features where notch control prevails; high-silicon ferritic grades for large, blunt features where defect tolerance is paramount. Overall, the method supports lighter, more reliable cast designs without resorting to overly conservative safety factors.

1. Introduction

Ductile cast iron (DCI), also referred to as nodular cast iron or spheroidal graphite iron, is increasingly recognized as a key structural material in modern industry. Its unique combination of mechanical strength, castability, and cost-effectiveness has led to widespread adoption in automotive, energy, cement production, and heavy machinery applications [1–3]. In many industrial cases, for large, complex, thick-walled components, DCIs can offer a cost-effective alternative to forged steel parts, owing to improved castability, lower machining allowances, and favorable material yields [4,5]. Their production flexibility enables the design of intricate shapes in a single casting step, minimizing machining requirements and material waste [6,7]. Furthermore, in a context where sustainability and resource efficiency are increasingly crucial, DCIs offer advantages in terms of lower energy consumption during processing and the potential for extended service life through defect-tolerant design [8].

However, predicting the fatigue performance of heavy-section components remains challenging, because their microstructure and defect population differ markedly from those of the thin or laboratory-scale castings typically examined in the literature. Slow solidification promotes the formation of microshrinkage porosity [9,10], whereas service-relevant geometries often incorporate pronounced stress raisers. Understanding how these two factors—intrinsic porosity and geometric notches—interact to control fatigue initiation is therefore essential for achieving safe, efficient, and defect-aware design of heavy-section DCI components. While macroporosity (on the order of centimeters) can be detected during quality control by non-destructive tests and generally predicted by casting simulation software, micro shrinkage porosity, with pore sizes up to a few millimeters, remains unavoidable in large castings and significantly more insidious [11,12]. These defects are often

* Corresponding author.
E-mail address: vigilio.fontanari@unitn.it (V. Fontanari).

https://doi.org/10.1016/j.ijfatigue.2025.109455
Received 5 November 2025; Received in revised form 10 December 2025; Accepted 19 December 2025
Available online 27 December 2025

Nomenclature

List of symbols

$2\overline{\alpha}$	Notch opening angle
E	Young's modulus
EB-HSV	Energy based highly stressed volume
G	Shear modulus
HB	Brinell hardness
HSV	Highly stressed volume
UTS	Ultimate tensile strength
V_0	Scanned volume in CT scans
V	Actual process volume
d_F	Feret diameter
F	Cumulative probability
$K_{f,P}$	Pore fatigue stress concentration factor
$K_{f,N}$	Notch fatigue stress concentration factor
K_f	Combined pore-notch fatigue stress concentration factor
R_1	Mode I SED control radius
χ_0	Volume scaling factor
ε_f	Strain at tensile failure
γ	Fitting parameter that correlates $K_{f,P}$ to d_F
λ	Shape parameter of the pores' statistical distribution
δ	Scale parameter of the pores' statistical distribution
σ_f^*	Intrinsic fatigue strength
σ_f	fatigue strength of unnotched specimens
σ_{HCF}	Combined pore-notch high cycle fatigue strength
$\sigma_{y,0.2}$	Yield strength

randomly distributed within the casting, and their morphology and density strongly depend on local thermal history, alloy composition, and melt treatment [13,14]. When located at critical stress regions, micropores act as stress concentrators and preferential sites for fatigue crack initiation [15,16]. Experimental evidence has demonstrated that their presence can reduce the fatigue strength of ductile irons by as much as 40 % compared to pore-free material [17]. Such a reduction is highly detrimental and limiting in safety–critical applications and compels designers to adopt conservative safety factors [18], ultimately limiting the efficiency and sustainability of the material.

The problem is compounded by the stochastic nature of microporosity. Unlike deterministic geometrical features such as notches or fillets, micropores vary in size, shape, and location in ways that are not easily predictable [14,19]. Foundry practices, including the use of chillers, exothermic sleeves, optimized feeding systems and proper melt treatment and inoculation can mitigate microporosity but cannot completely prevent its formation in heavy castings [2,20]. Moreover, commercial casting simulation software, while effective in predicting macroporosity, fails to predict the onset of microporosity [13]. Most of these tools rely on simplified thermal analyses and semi-empirical criteria —for example, the Niyama criterion [21], originally calibrated on steel castings and therefore not fully representative of the distinct solidification behavior of DCIs [22,23]. As a result, designers often cannot anticipate the size and distribution of micropores in a given casting, leading to overly conservative designs that penalize weight and cost efficiency.

From a structural-design standpoint, the implications are substantial. The conventional workflow compares FE-computed peak stresses with S–N data from smooth, defect-free specimens [18]. In practice, this folds the effect of casting defects into an "intrinsic" material property and neglects stress-gradient effects, which are decisive for whether a pore located near a notch or surface irregularity will trigger fatigue damage [17]. As a result, traditional checks can be non-conservative—e.g., treating pores in a notched hotspot as if they behaved like those in plain specimens—or overly conservative—e.g., using plain-specimen data from small laboratory castings whose defect population differs markedly from that of a thick-walled component [24]. Both situations degrade prediction quality and lead to suboptimal material utilization.

To overcome these limitations, several defect-sensitive approaches have been developed. Murakami's $\sqrt{\text{area}}$ model remains a cornerstone, providing a first-order approximation of the fatigue limit as a function of the projected area of the most critical defect [25,26]. Although highly influential, this model does not fully capture defect–notch interactions or stress gradient effects. Statistical treatments, particularly extreme value statistics (EVS) [27,28], have been successfully used to estimate the largest expected defect in a stressed volume and link it to fatigue strength [29–32]. At the same time, approaches based on the theory of critical distances (TCD) [33] and strain energy density (SED) [34] have been employed to model the role of stress gradients around notches and microdefects. Originally developed for defect-free metals, these methods have recently been adapted to defect-sensitive materials such as cast irons, showing good predictive capability [35–37].

Recent contributions from our group have integrated CT-based defect characterization, EVS, and SED into an energy-based definition of the highly stressed volume (EB-HSV), providing a useful framework to link the effect of defect population to that of geometric stress raisers [17]. This methodology successfully predicted whether fatigue failure would be dominated by notches or pores in pearlitic ductile iron EN-GJS-600–3 (GJS-600–3) and was validated against experimental fatigue data [17]. Nevertheless, significant questions remain open.

High-silicon ferritic ductile cast irons (HSi grades) have received limited attention in defect-sensitive fatigue studies, despite their increasing industrial relevance [15,38]. Their ferritic matrix, stabilized and strengthened by silicon, provides good ductility and oxidation resistance, along with lower notch sensitivity compared to pearlitic grades [39,40]. While pearlitic DCIs generally exhibit higher fatigue strength when failure is governed by matrix hardness, nodule morphology, or graphite distribution—as is typically the case in thin or small castings where shrinkage porosity is rare—HSi grades may outperform them in pore-dominated regimes characteristic of thick-walled components. Although the intrinsic fatigue strength of HSi is lower, their potentially higher tolerance to microshrinkage porosity makes them attractive candidates for large heavy-section castings [36,38]. Nevertheless, comparative studies that directly assess pearlitic GJS-600–3 and HSi grades under identical casting, defect, and loading conditions remain scarce [36].

The present work advances the fatigue characterization of ductile cast irons through a comparative investigation of the plain and notched fatigue strengths of EN-GJS-600–3 (pearlitic) and HSi (high-silicon ferritic) grades. Unlike most studies, which focus on thin or small castings (see for instance [6,15 38]), this work examines microstructural conditions representative of thick-walled components, where cooling rates and defect populations differ substantially. High-resolution X-ray CT is used to quantify pore size distribution, morphology, and spatial arrangement in both grades, and extreme-value statistics (EVS) are employed to estimate the critical defect expected within the energy-based highly stressed volume (EB-HSV). Local stress concentration effects are evaluated through SED-based finite element analyses. By extending the EB-HSV/SED framework originally developed for GJS-600–3 in [17], the present study provides a mechanistic and quantitative separation between pore-dominated and notch-dominated regimes, enabling the first geometry- and defect-aware comparison of the fatigue performance of these two technologically important DCI grades. This unified approach clarifies in which design scenarios each material is expected to outperform the other and leads to a simplified, design-ready criterion that incorporates the competitive nature of geometric stress

raisers and intrinsic porosity—thereby offering a more robust basis for material selection and fatigue assessment in heavy-section DCI components.

The paper is structured as follows. Section 2 describes the investigated materials, casting conditions, CT-based pore characterization, statistical modelling, and uniaxial fatigue testing. Section 3 introduces the SED-based finite element framework used to determine intrinsic fatigue properties and to quantify local stress concentration effects associated with the pore population. Section 4 integrates these elements within the EB-HSV approach to evaluate the competition between notch- and pore-driven initiation and validates the framework against experimental results across notch severities. Section 5 translates these findings into simplified, design-oriented guidelines for engineering use. Section 6 positions the proposed methodology within the context of classical defect-sensitive fatigue models, including a comparison through Kitagawa–Takahashi diagrams. Finally, Section 7 summarizes the main conclusions and outlines directions for future research.

2. Material and experimental characterization

Standards for DCIs classify grades primarily by tensile properties measured on machined specimens, with an additional impact requirement for grades intended for low-temperature service. Because these properties are sensitive to solidification and cooling time, the optimal chemistry for a given grade depends on the size and geometry of the casting. In large sections, the response within the elastic range up to yield is relatively stable; however, post-yield behavior and ductility are strongly section-dependent. Given that our objective is to compare a pearlitic DCI with a high-silicon, solution-strengthened ferritic (HSi) DCI, the chemical compositions were selected to meet target yield strengths for the respective grades. For the pearlitic grade, it is important to note that the ultimate tensile strength in thick-section castings is typically lower than the nominal values specified by standards. This reduction stems from diminished ductility and, consequently, a smaller strain-hardening contribution to fracture strength—effects that are not fully captured by current standards.

The study considers two materials: a pearlitic EN-GJ-600–3 (hereafter GJS-600–3) and a silicon-solution-strengthened ferritic ductile iron (hereafter HSi). The HSi grade was engineered to sit between EN-GJS-450–18 and EN-GJS-500–10 in both composition and mechanical response, and is treated here as a single representative ferritic variant. The chemical compositions and main mechanical properties of the two DCI grades are reported in Table 1. All the tested specimens were extracted from a large cast cylinder with 300 mm diameter and 520 mm height, whose cooling rate was defined to reproduce that of a thick-walled cast as described in [17].

Fig. 1 compares the microstructures of the two DCI grades, emphasizing the distinct distribution and morphology of the graphite nodules. The GJS-600–3 grade exhibits a predominantly pearlitic matrix with ferritic zones, mainly surrounding the nodules, whereas the HSi grade shows a fully ferritic microstructure.

Metrological X-ray CT was exploited to evaluate the statistical distributions of both graphite nodules and shrinkage pores inside the two investigated DCI grades, analyzing a scanned volume $V_0 = 504\ mm^3$ and $V_0 = 650\ mm^3$ in GJS-600–3 and HSi, respectively. The analyses were conducted using a Nikon Metrology MCT225 system (Nikon Metrology, UK) characterized by a micro-focus X-ray source (minimum focal spot size equal to 3 μm), 16-bit flat panel detector with 2000 × 2000 pixel grid, and temperature-controlled cabinet (20 ± 0.5 °C). The voxel size was set equal to 5.8 μm. The obtained CT reconstructions are shown in Fig. 2.

All CT-scanned specimens were extracted from the same thick-walled casting and underwent similar cooling histories, ensuring that the resulting porosity is representative and statistically uniform throughout the volume of interest. Therefore, the objective of the CT investigation is not to map the spatial distribution of defects, but to obtain an accurate statistical characterization of pore size and morphology. This information, together with EVS, enables the estimation of the most critical defect expected in any highly stressed volume, which is the quantity directly controlling fatigue initiation in the proposed model.

CT analyses revealed two distinct porosity signatures: the pearlitic GJS-600–3 contains relatively few but larger pores with random spatial locations, whereas the ferritic HSi contains many smaller pores distributed more uniformly throughout the volume. Representative 3D reconstructions of shrinkage pores are shown in Fig. 3. Pores in the HSi grade exhibit a markedly more irregular morphology than those in GJS-600-3, with sharper concavities and branching features suggesting higher surface-to-volume ratios.

As reported in [17] the Feret diameter was adopted as geometrical parameter to describe the statistical distribution of the shrinkage pores. The CT data were analyzed adopting the statistics of the largest extreme value distribution (LEVD) using the Maximum Likelihood Method [41], thus using the following expression, as function of the pore's Feret diameter (d_F):

$$d_F = \lambda + \delta(-\ln(-\ln(F))) \tag{1}$$

Where λ and δ are the shape and scale parameters, respectively, and F is the cumulative probability. The fitted statistical distributions are shown in Fig. 4.

At a fixed Feret diameter, pores in the HSi grade exhibit more complex (less spherical) geometries and smaller volumes, implying higher surface area, whereas pores in GJS-600-3 are smoother and bulkier, with lower surface area. Consistent with this, Fig. 4 shows that HSi contains a denser pore population; however, the largest pores—those most relevant for fatigue initiation—are generally smaller in HSi than in GJS-600–3.

Uniaxial fully-reversed (stress ratio R = −1) load-controlled fatigue tests were performed on axisymmetric V-notched specimens whose geometry is shown in Fig. 5. Briefly, the specimen set spans a controlled transition from a sharp V-notch (the opening angle $2\overline{\alpha}$ in Fig. 5a is 60°) toward a plain (shown in Fig. 5b, $2\overline{\alpha}$ virtually 180°) geometry by progressively increasing the notch opening angle $2\overline{\alpha}$ (100°, 140°, 160°, 170°), thereby systematically reducing notch severity.

The results of the experiments obtained on the GJS-600–3 cast iron grade are reported in [17]. Consistent with that study, the S–N data obtained for the HSi grade (Fig. 6a) were fitted using the asymptotic Stromeyer equation [42]:

$$\sigma_{N,a} = k_1 + \frac{k_2}{N_f^{k_3}} \tag{2}$$

Table 1
Chemical composition and main static mechanical properties of the investigated DCI grades. $\sigma_{y,0.2}$: 0.2% yield stress, UTS: ultimate tensile strength, ε_f: total deformation at failure, HB: Brinell hardness.

%	C	Si	Mn	P	S	Cu	Ni	Mg
GJS-600–3	3.55	2.39	0.28	0.038	0.009	0.52	0.02	0.046
HSi	3.43	3.57	0.19	0.04	0.009	0.06	0.02	0.043
				$\sigma_{y,0.2}$ (MPa)	UTS (MPa)	ε_f (%)	HB	
GJS-600–3				363 ± 8	485 ± 15	2.1 ± 0.5	198 ± 4	
HSi				376 ± 8	482 ± 7	12.0 ± 3.1	176 ± 4	

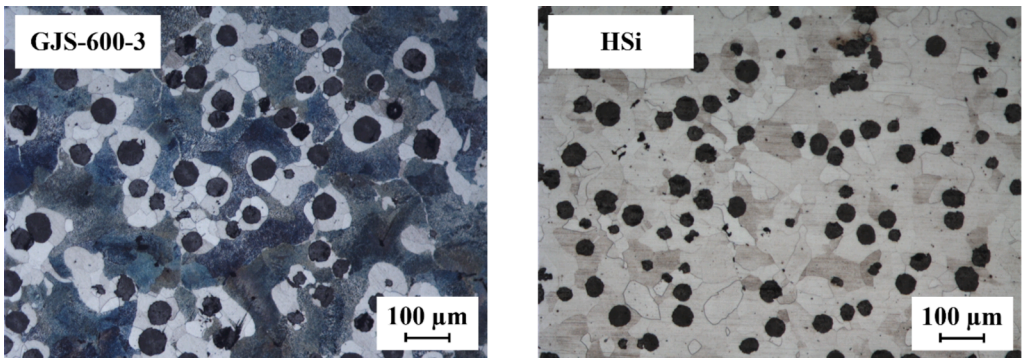

Fig. 1. A) mainly pearlitic microstructure of gjs-600–3, b) fully ferritic microstructure of HSi.

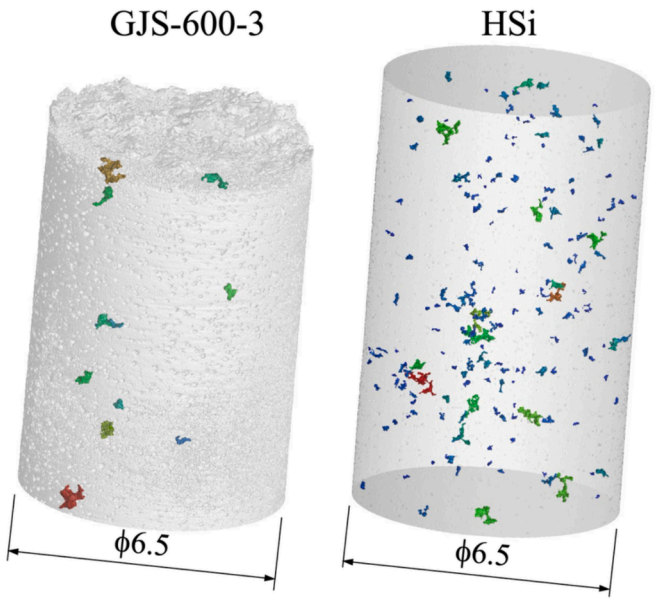

Fig. 2. CT detection of microshrinkage porosity (coloured spots) in the two investigated DCI grades. Clear differences in pore amount, size and morphology are evident between the materials.

which provides a smooth transition between the finite-life and endurance-limit regimes and accurately captures the knee exhibited by the experimental S–N trends. This functional form is widely used for cast irons and other materials that exhibit a pronounced asymptotic fatigue limit. The fitting parameters k_1, k_2, k_3 are listed in Table 2 along with standard deviation. The goodness-of-fit was excellent for all SN curves, with $R^2 = 0.99$ and low, randomly distributed residuals across the full lifetime range, confirming the suitability of the Stromeyer model for the present dataset. The fitted curves are shown in Fig. 6a for a 50 % failure probability (solid line), with 10 % and 90 % probability bounds indicated by the colored scatter band.

Fig. 6b compares the 50 % failure-probability S–N curves of the two DCI grades for (i) plain specimens and (ii) sharp V-notched specimens (60° opening angle, root radius $R = 0.2$ mm), which represent the most severe notch condition investigated. A clear reversal in fatigue strength is observed when moving from the plain to the sharply notched condition: the grade superior in the plain configuration becomes inferior under the sharp notch, and vice versa. To elucidate the underlying mechanisms, detailed SEM fractography was performed on both plain and notched specimens, focusing on how notch severity and micro-shrinkage pores jointly govern crack initiation and early propagation across the tested geometries.

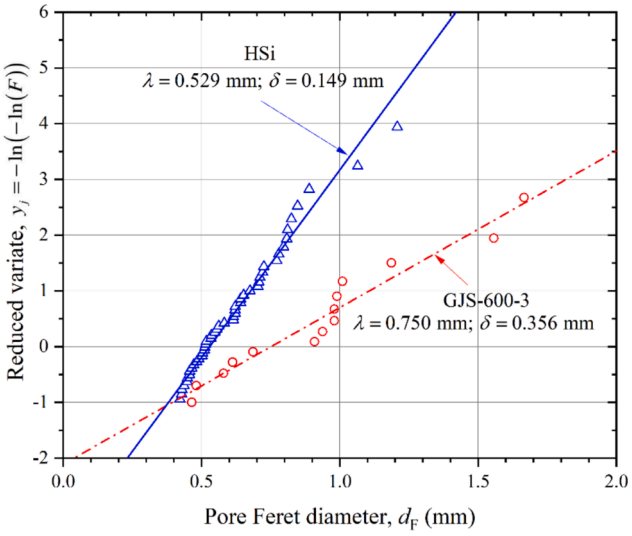

Fig. 4. Statistical distributions of Feret diameter of shrinkage pores collected by CT scans for the investigated materials. λ and δ are shape and scale parameters of the cumulative probability function expressed by Eq. (1).

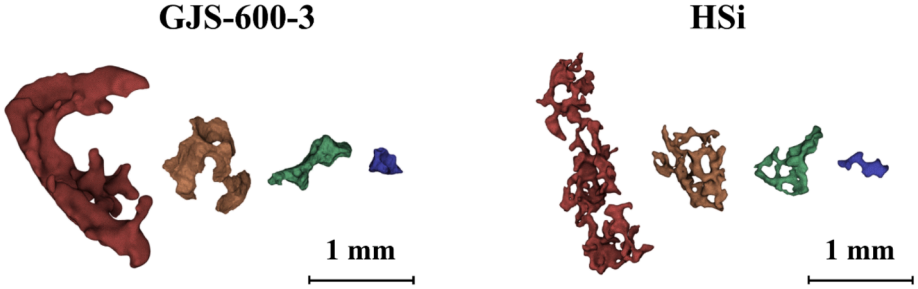

Fig. 3. CT 3D reconstructions of shrinkage pores showing different morphologies for the two investigated DCI grades.

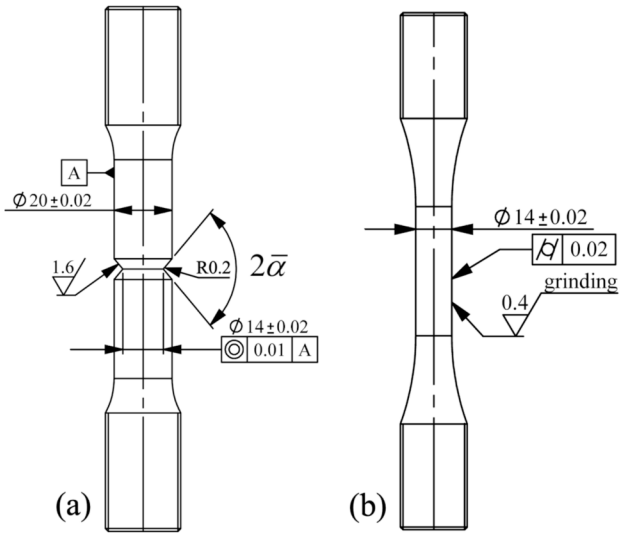

Fig. 5. Technical drawings of the specimens used in fatigue axial tests: (a) V-notched specimens with variable opening angle angle $2\bar{\alpha}$ of 60°, 100°, 140°, 160°, 170°; (b) plain specimen with a gage diameter of 14 mm.

3. Sed-based modeling of notch effects associated to pores population

The 3D reconstruction of some shrinkage pores extracted from CT scan were used to create finite element models, where single pores are randomly rotated and placed in a plain specimen with 14 mm diameter and rotated to assume different configurations with respect to the loading direction. The same approach was already presented in [17] for GJS-600–3 grade. This work integrates the analysis with the data related to the HSi DCI grade.

Finite-element results were interpreted using a strain-energy–density (SED) approach to quantify the influence of pores on fatigue strength. In this framework, the SED is volume-averaged over a control region (torus of radius R_1) centered on the pore hotspot, i.e., the location experiencing the most severe local stress state. For this purpose, a prior calibration of the matrix intrinsic fatigue strength and the associated control radius R_1 is required before evaluating pore effects. An inverse search procedure based on the knowledge of the fatigue strength of at least two V-notched axisymmetric specimens is adopted. This strategy, explained in [43], aims to eliminate the influence of intrinsic pores and produces a reliable estimate of the intrinsic fatigue strength of the matrix (σ^*_{fl}), including the effects of microstructure and graphite nodules. For GJS-600–3, the inversion procedure follows [17] and uses two 60° V-notched geometries that differ only in root radius ($R = 0.2$ and 1 mm). This strategy was not adopted for HSi because the two 60° variants exhibited nearly identical fatigue strengths, rendering the inversion ill-conditioned and thus not robust. Instead, for HSi we employed three V-notched geometries with opening angles of 60°, 100°, and 140°. As shown later, these cases lie in a notch-controlled regime (i.e., not governed by microporosity-triggered initiation), which provides a more reliable basis for inversion.

The results of this inversion method are summarized in Table 3 together with the values of fatigue strength (σ_{fl}) measured on plain specimens. Interestingly, the σ^*_{fl} values are in very good agreement with those estimated in [38] for DCI grades with fully pearlitic and fully ferritic microstructures and negligible effects of micro-shrinkage porosity.

The detailed description and the flow chart representing the SED-based procedure for FE modelling of the critical fatigue stress concentration factor $K_{f,P}$ in each of the pore configurations inside the tested volume is reported in [17]. In brief, the model is meshed, and the volume is loaded with unitary remote stress. At local stress maxima around the pore a spherical control volume of radius R_1, centered at the peak of maximum principal stress, is defined over which the mean SED is evaluated. The procedure is iterated until the whole surface of the pore is covered. The maximum evaluated SED, regarded as SED_{max}, is taken as representative of the analyzed pore and used to calculate the pore's fatigue stress concentration factor $K_{f,P}$ according to the following

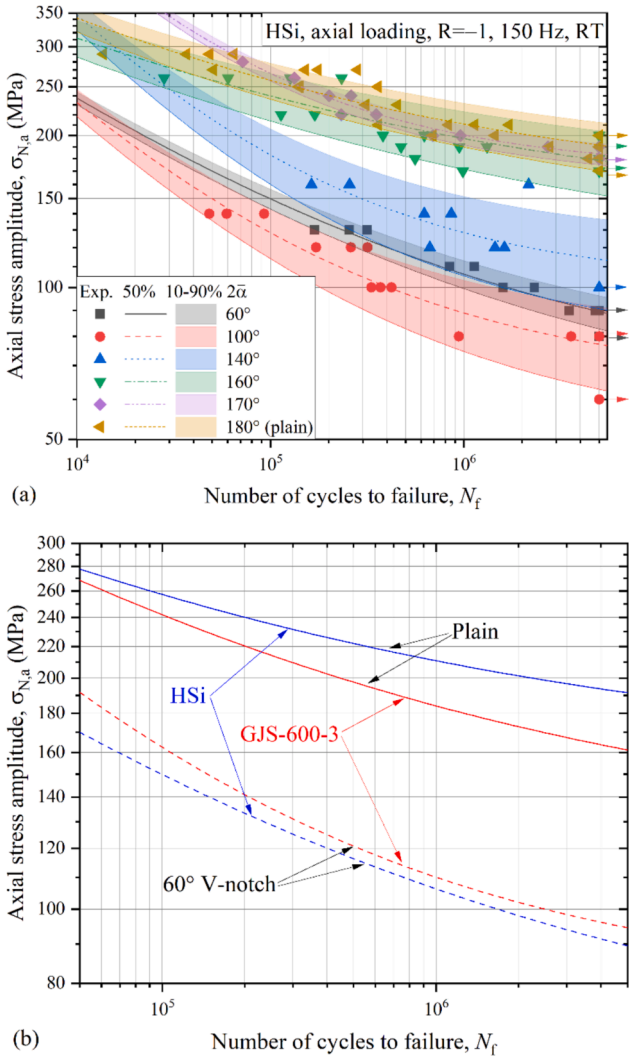

Fig. 6. (a) Axial SN fatigue curves on plain and V notched specimens made of HSi DCI. b) Comparison between 50% failure probability SN curves obtained on plain and s notched specimens (opening angle 60°) made of HSi and GJS600 DCI grades. The SN curves are obtained through interpolation of Equation (2) whose best-fit coefficients are listed in Table 2.

Table 2
Best fit coefficients of Eq. (2) used to interpolate the SN curves on HSi grade as explained in [17]. S is the standard deviation. σ_{fl} is the fatigue strength at $5 \bullet 10^6$ cycles.

Specimen geometry	k_1 (MPa)	k_2 (MPa)	k_3	S (MPa)	σ_{fl} at $5 \bullet 10^6$ cycles
Plain specimen (180°)	155	2081	0.261	16.5	191
170°	171	32,247	0.506	7.0	184
160°	138	1490	0.233	20.2	179
140°	101	19,833	0.477	18.0	114
100°	65	8144	0.422	11.2	77
60°	63	2833	0.303	5.3	90

Table 3
Plain fatigue strength σ_{fl} , i ntrinsic fatigue strength σ^*_{fl}, SED control radius R_1 inferred by the inversion procedure at $5 \bullet 10^6$ cycles.

DCI grade	$\sigma_{fl}(MPa)$	$\sigma^*_{fl}(MPa)$	$R_1(mm)$	Sensitivity to pores
GJS-600–3	161 ± 10	277 ± 25	0.15	High
HSi	191 ± 16	235 ± 25	0.16	Low

expression:

$$K_{f,P} = \sqrt{\frac{SED_{max}}{SED_{nominal}}} = \sqrt{\frac{SED_{max}}{\frac{\sigma^2_{nominal}}{2E}}} \tag{3}$$

where $\sigma_{nominal} = 1$ MPa is the applied unitary nominal stress, and E is the elastic modulus. In total, 200 GJS-600–3 and 40 HSi randomly embedded pore configurations were analyzed in a plain specimen with a 14 mm gauge diameter.

Fig. 7 reports the cumulative distributions of the probabilistic fatigue notch factor, $K_{f,P}$, for the two DCI grades. A clear separation emerges: the HSi grade exhibits a noticeably steeper cumulative curve—consistent with a predominance of medium-to-low $K_{f,P}$ values—and its upper tail is truncated, with significantly lower extreme $K_{f,P}$ values than those of GJS-600–3.

Following the classification approach reported in [17] that relates $K_{f,P}$ to the Feret diameter d_F of the pore, the data were then fitted according to the following power-law equation [42]:

$$K_{f,P} = \left(\frac{d_{F,pore}}{d_{F,nodule}}\right)^{\gamma} \tag{4}$$

where $d_{F,pore}$ is the pore's Feret diameter, $d_{F,nodule}$ is the graphite nodules maximum Feret diameter, and γ is a fitting parameter. The maximum $d_{F,nodule}$ assessed by analyzing the data coming from the CT scans are equal to 160 μm for the GJS-600–3 grade, and 67 μm for the HSi grade. Notch effect of pores is assumed as irrelevant when $d_{F,pore} \leq d_{F,nodule}$ (Fig. 8).

The finite element simulations show that the HSi grade is considerably less sensitive to shrinkage pores compared to the GJS-600–3 grade. This phenomenon is explained by two main reasons: (i) the SED control radius of the HSi grade is slightly larger than the GJS-600-3's one, making the material less sensitive to geometrical discontinuities. This is reasonable, as the ferritic matrix is characterized by a ductile behavior,

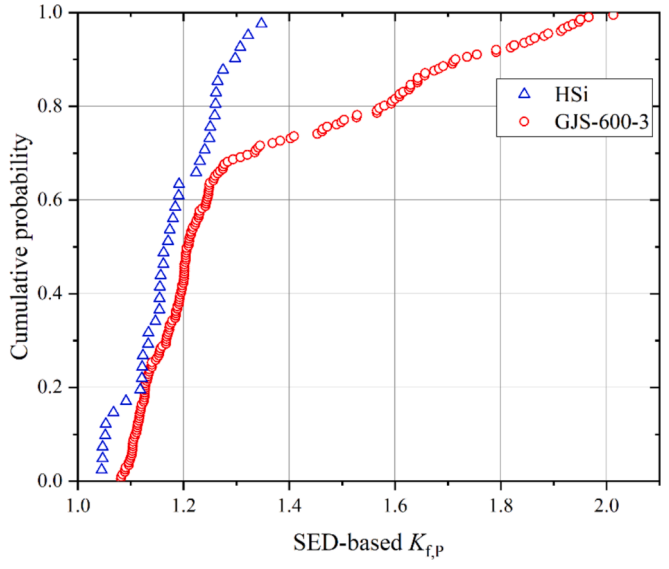

Fig. 7. Cumulative curves of the pore fatigue stress concentration factor $K_{f,P}$ calculated for the two DCI grades.

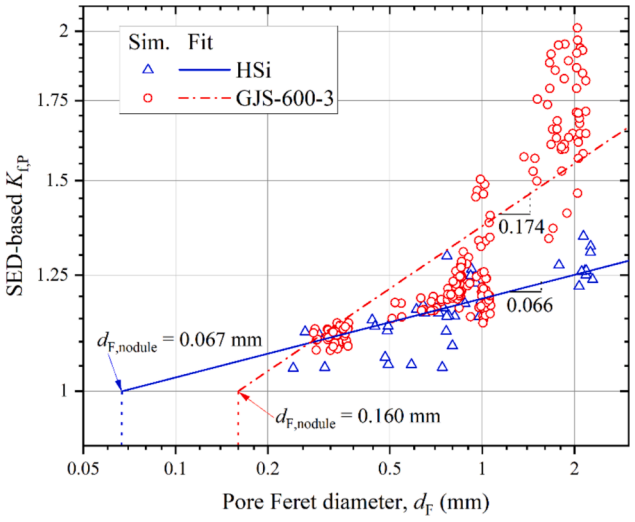

Fig. 8. Fatigue stress concentration factor at pores as function of the pore's size, for the two investigated materials. The numerical data were fitted using the power-law model expressed in Eq. (4), with the exponent γ represented by the slope of the double-logarithmic plot.

as confirmed by the elongation at fracture (ε_f) reported in Table 1, (ii) the peculiar morphology of HSi grade's shrinkage pores, characterized by a large surface area and small volume, is producing less severe stress intensification, thus decreasing the impact of pores on the fatigue properties of the material.

4. Probabilistic evaluation of notch-pores interaction

The Feret diameter represents a possible choice of dimensional parameter to be used to estimate the expected pore size in a sampled volume of material. For this purpose, extreme value statistics based on the maximum likelihood criterion are used. If V_0 indicates the volume subjected to CT scan on which the pore population was identified, V is the given volume on which the expected pore size must be estimated as a function of the cumulative probability, the Makkonen et al. [44] model based on the scaling factor χ_0 can be adopted:

$$d_F(F,V) = [\lambda + \delta(-\ln(-\ln(F)))] \bullet \chi_0$$
$$\chi_0 = \begin{cases} \dfrac{d_F(F,V)}{d_F\left(F^{\frac{V}{V_0}}\right)} & V \leq V_0 \\ \dfrac{d_F\left(F^{\frac{V_0}{V}}\right)}{d_F(F,V)} & V > V_0 \end{cases} \tag{5}$$

As elucidated in [17], the maximum expected pore size is taken at $F = 0.99$, and the volume V is defined as the highly stressed volume (HSV). This is defined as the set of material points where the local stress lies within the "effective" notch-controlled window bounded above by the hotspot peak and below by the pore-reduced threshold:

$$V = \{\, \mathbf{x} \in \Omega : \ \frac{\sigma_{peak}}{K_{f,P}} \leq \sigma \leq \sigma_{peak} \,\} \tag{6}$$

Intuitively, V is the region that is (i) driven by the notch stress field and (ii) still sufficiently highly loaded that an embedded pore could interact with—and potentially govern—crack initiation. Since this definition is related to the energy based (EB) evaluation of the fatigue stress concentration factor $K_{f,P}$ the calculated volume is defined as EB-HSV.

The unknown values of $d_F(0.99, V)$, $K_{f,P}$ and EB-HSV V, mutually linked through transcendental equation, can be evaluated with an iterative procedure elucidated in [17], starting from a first guess of $K_{f,P}$.

Convergence is usually reached in a few iterations. Once $K_{f,P}$ has been calculated, the pore-dominated fatigue strength can be deduced from the intrinsic fatigue properties of the pore-free matrix (σ_f^*):

$$\sigma_{fl} = \frac{\sigma_{fl}^*}{K_{f,P}} \tag{7}$$

Fig. 9 shows the predicted fatigue limit from Eq. (6) as a function of the EB-HSV, evaluated at a cumulative probability $F = 99\%$. As the EB-HSV increases, the largest defect expected within that volume also increases, leading to a higher probabilistic pore fatigue stress concentration factor $K_{f,P}$. Based on the pore population, the ferritic HSi grade is less sensitive to the sampling volume, while GJS-600–3 significantly improves its response as the probability of finding large critical pores within the EB-HSV decreases. Our predictions indicate a crossover behavior: once the EB-HSV exceeds a few hundredths of mm^3, the fatigue limit of the ferritic HSi grade becomes higher than that of the pearlitic GJS-600–3. Although this may appear counterintuitive given the higher intrinsic fatigue strength of GJS-600–3, it is explained by the greater pore sensitivity of the pearlitic matrix. Note that the two curves are not deterministic; their uncertainty is expected to be comparable to the scatter bands of the experimentally determined fatigue limits for the two DCI grades, so the crossover region spans roughly 2–3 orders of magnitude in EB-HSV. For reference, Fig. 9 also reports the predicted fatigue limits for plain specimens (diameter 14 mm, gauge length 50 mm), corresponding to an EB-HSV of 7696.9 mm^3. These predictions agree with the plain fatigue limits in Table 2, with an error of about 1 % for both grades. Further validation of the approach is provided in [17], where a FEM analysis of a failed specimen—using the CT-identified critical pore location and SEM-determined initiation site—confirms the model's predictions.

Up to this point, the model explicitly addresses the effect of microshrinkage pores on fatigue. Although the notch influences the EB-HSV definition, its direct contribution to crack-initiation resistance has not yet been quantified. An analogous SED-based assessment can be carried out for the notch itself. The detailed procedure is described in [17]. In brief: (i) build an elastic FE model of the notched geometry; (ii) apply a unit nominal stress $\sigma_{nom} = 1$; (iii) evaluate the averaged SED in a control volume of radius R_1 centered at the notch root; and (iv) compare this to the reference SED for a smooth specimen under the same nominal loading. The corresponding notch fatigue stress concentration factor $K_{f,N}$ is then obtained according to the following equation.

$$K_{f,N} = \sqrt{\frac{SED_{notch}}{SED_{nominal}}} = \sqrt{\frac{SED_{notch}}{\frac{\sigma_{nominal}^2}{2E}}} \tag{8}$$

In components containing both geometric stress raisers and intrinsic microshrinkage pores, the mechanism that produces the larger fatigue stress-concentration factor—either the notch ($K_{f,N}$) or the pore ($K_{f,P}$)—is expected to govern crack initiation and, hence, the fatigue strength. To experimentally validate this competition, Fig. 10 plots the high-cycle fatigue strength versus notch opening angle for both DCI grades, alongside the two bounding predictions: (i) pore-dominated behavior, $\sigma_{fl}^*/K_{f,P}$ (dash-dot lines), and (ii) notch-dominated behavior, $\sigma_{fl}^*/K_{f,N}$ (solid lines). The two materials exhibit distinct crossover behavior. For GJS-600–3, the data follow the notch-controlled branch at small and intermediate opening angles and cross to the pore-controlled branch at $\sim 160°$, indicating that as the notch becomes blunt and the stress gradient relaxes, the largest pore expected in the EB-HSV governs initiation. In contrast, for the HSi grade the transition to pore control occurs only for very blunt geometries ($\gtrsim 170°$), i.e., when the elastic stress concentration factor K_t approaches unity. This delayed transition reflects the higher defect tolerance of the ferritic matrix. In Fig. 10, the regime change is emphasized by switching line thickness at the intersection point, marking where the governing mechanism switches from notch to pore. The model also reproduces the plain-specimen fatigue limits well, as already shown in Fig. 9. We note, however, that it enforces a sharp switch between pore- and notch-controlled regimes—a useful idealization but not fully physical, since it imposes a deterministic boundary in a region where stochastic effects (defect occurrence, size, and location) dominate. Consistently, the largest experimental scatter appears near this transition, indicating a gradual rather than abrupt mechanism change. Despite this simplification, the design implications are clear: for very blunt notches (large EB-HSV, pore-controlled), HSi attains the higher fatigue limit due to its greater defect tolerance; for

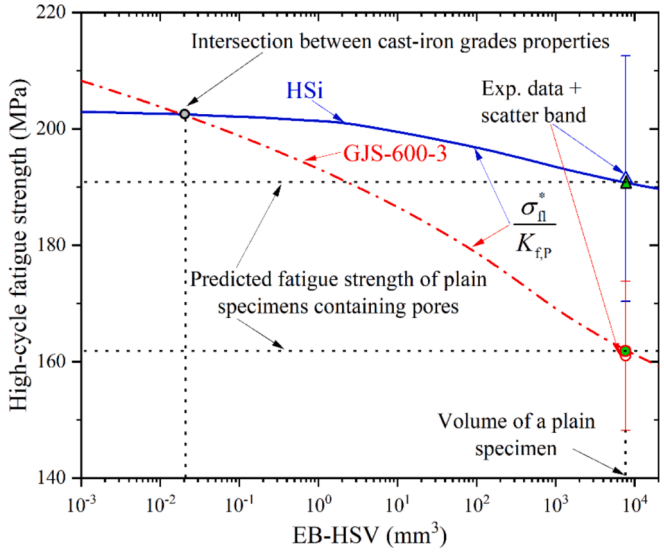

Fig. 9. Fatigue strength of the material, containing shrinkage pores, as a function of the highly stressed volume EB-HSV. Mean value and scatter band of the fatigue limits found on plain specimens of both DCI grades are indicated for comparison (GJS-600–3 in red; HSi in blue). The green symbols indicate the plain-fatigue-strength values predicted for the EB-HSV corresponding to the plain specimens tested in this work.

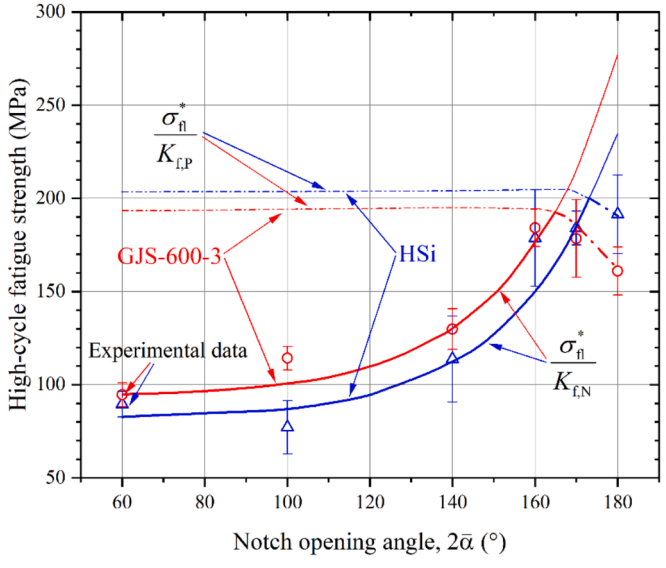

Fig. 10. High-cycle fatigue strength versus notch opening angle $2\bar{\alpha}$ for the two DCI grades (GJS-600–3 in red; HSi in blue). Symbols: experimental results (with scatter bars). Lines: model predictions assuming (i) pore-dominated initiation, $\sigma_{fl}^*/K_{f,P}$ (dash-dot), and (ii) notch-dominated initiation, $\sigma_{fl}^*/K_{f,N}$ (solid). The governing mechanism at each angle is indicated by the thicker segment of the corresponding curve. A crossover from notch to pore control occurs for GJS-600–3 at $\sim 160°$, whereas for HSi pore control emerges only for very blunt geometries ($\gtrsim 170°$, i.e., $K_t \to 1$).

more severe notches (small EB-HSV, notch-controlled), GJS-600–3 leverages its higher intrinsic fatigue strength and outperforms HSi.

Recent literature has shown that the specific notch type and geometry can strongly influence fatigue behavior by altering local stress gradients, plastic-strain localization, and microstructural constraint conditions. For example, He et al. [45] used crystal-plasticity modeling to demonstrate how different notch profiles in Ni-based alloys modify the extent of strain concentration and shift the preferred crack-initiation paths. Likewise, the study reported in [46] highlights how sharper or more acute notches intensify stress concentrations and promote earlier crack initiation. In our work, these effects manifest through the EB-HSV: sharper notches reduce the EB-HSV, making initiation more sensitive to intrinsic matrix properties, whereas blunter notches enlarge this volume and increase the likelihood that fatigue initiation becomes pore-controlled. Unlike the aforementioned studies, which examine notch effects in nominally defect-free materials, our results reveal how notch geometry and shrinkage-pore statistics jointly determine the governing initiation mechanism in thick-section ductile irons. This provides a mechanistic explanation for the progressive transition observed in Fig. 10 and underscores the need to consider both stress-gradient effects and defect populations in defect-sensitive fatigue assessments.

SEM fractography on representative specimens confirms that shrinkage pores are the preferred crack-initiation sites in plain and mildly notched conditions for both GJS-600–3 and HSi. Conversely, for sharp V-notches, cracks initiate at the notch root, with early propagation guided by the local graphite nodule morphology. Figs. 11 and 12 compile fracture surfaces across notch severities for GJS-600–3 and HSi, respectively. For both materials, the 160° opening angle exhibits a mixed initiation regime: in most specimens the graphite structure at the notch root triggers initiation, yet pore-assisted initiation is also observed in the near-root region—consistent with our earlier observation that the switch from notch- to pore-controlled initiation is not abrupt but gradual across a transition band of notch severities (EB-HSV). This mixed behavior is more pronounced in GJS-600–3.

Taken together, the mechanical results, modeling, and fractography indicate that material choice should be geometry- and volume-aware. GJS-600–3 performs slightly better in configurations with sharp notches (small EB-HSV), where its higher intrinsic fatigue strength prevails. Conversely, HSi benefits from a less detrimental pore population and becomes the preferable option for components with blunt notches and large highly stressed volumes, even though its ferritic matrix has a lower intrinsic fatigue strength than the pearlitic matrix of GJS-600–3. Consistent with the fractographic evidence, this switch in governing mechanism is gradual, occurring across a transition band of notch severities rather than at a single angle.

Fig. 13 reinterprets Fig. 9 by plotting the high-cycle fatigue strength

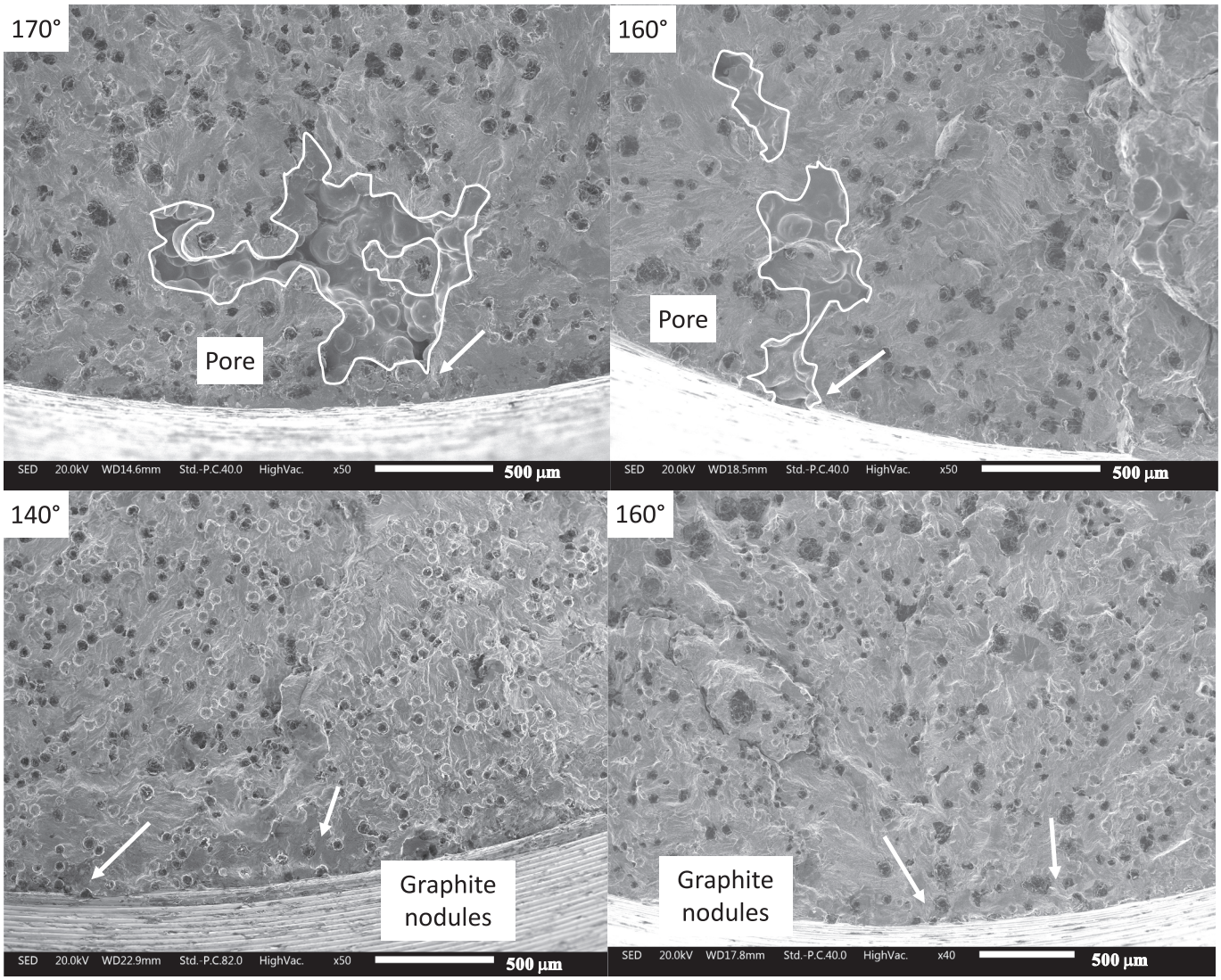

Fig. 11. SEM fracture surfaces of GJS-600–3 specimens with different notch severities. The notch opening angle is indicated in the top-left corner of each image.

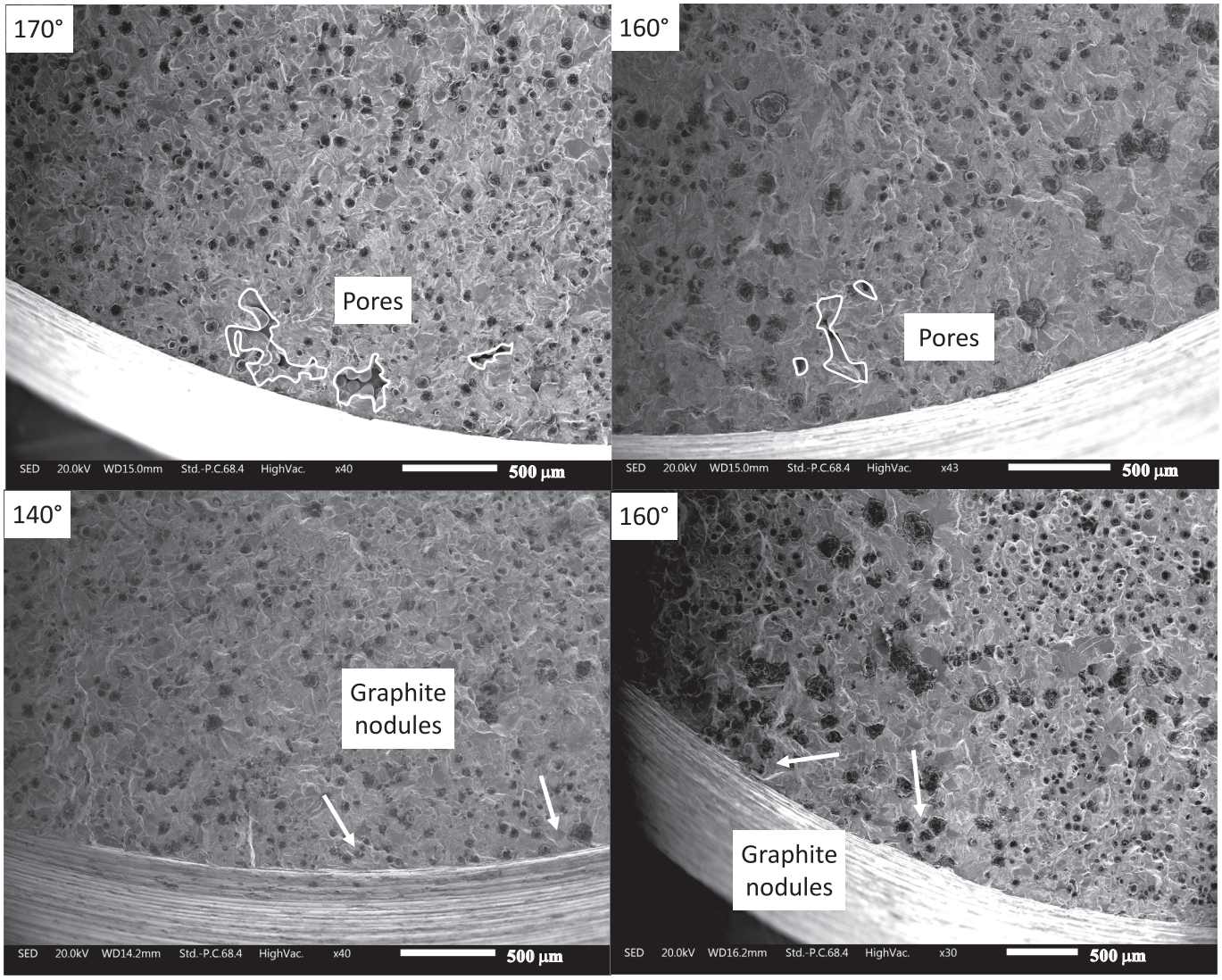

Fig. 12. SEM fracture surfaces of HSi specimens with different notch severities. The notch opening angle is indicated in the top-left corner of each image.

of each experimental variant against the energy-based highly stressed volume (EB-HSV) for (a) HSi and (b) GJS-600–3. Three regimes are delineated by the relative magnitude of the fatigue stress-concentration factors due to the notch ($K_{f,N}$) and to the pore ($K_{f,P}$):

(i) notch-dominated region where $K_{f,N} > K_{f,P}$;
(ii) a transition region centered on the condition $K_{f,N} \approx K_{f,P}$;
(iii) a pore-dominated region where $K_{f,P} > K_{f,N}$.

Within the transition band, a conservative lower bound is indicated by assuming full interaction between notch and pore, i.e., a multiplicative combination of their effects. Since in the transition region $K_{f,N} \approx K_{f,P}$, the bound reduces to dividing the intrinsic fatigue limit by the square of the pore factor,

$$\sigma_{fl} \approx \frac{\sigma^*_{fl}}{K_{f,N} K_{f,P}} \quad \underset{K_{f,N} \approx K_{f,P}}{\rightarrow} \quad \frac{\sigma^*_{fl}}{(K_{f,P})^2} \tag{9}$$

Above the transition (large EB-HSV), pore control prevails; below it (small EB-HSV), notch control governs—consistent with the crossover behavior discussed for Fig. 10. Note that the 160° and 170° notched variants lie in Fig. 13 within the transition band ($K_{f,N} \approx K_{f,P}$). This placement is consistent with SEM fractography, which shows concurrent notch-root and pore-assisted initiation—i.e., a mixed mechanism in this EB-HSV range. Conversely, the 60°, 100°, and 140° variants plot within the notch-dominated region ($K_{f,N} > K_{f,P}$), in line with the expectation that sharper notches (smaller EB-HSV) are governed by notch-root control.

Fig. 13 can be also used as a design map. For a given component:

1. Evaluate geometric effects with the SED approach (Section 4) to obtain $K_{f,N}$ for the notch(es) and compute the EB-HSV of the hotspot.
2. Locate the working point on Fig. 13 using the EB-HSV on the abscissa and the nominal high-cycle fatigue strength on the ordinate (initially neglecting pores when estimating the strength).
3. If the point falls in the notch-dominated region ($K_{f,N} > K_{f,P}$): the notch governs; the predicted fatigue strength $\sigma^*_{fl}/K_{f,N}$ can be used directly for design—no further pore analysis is needed.
4. If the point falls in the pore-dominated region ($K_{f,P} > K_{f,N}$; full square in Fig. 12): pores govern; design must be based on the critical pore expected in the EB-HSV. The working point is shifted (arrow in Fig. 13) to the pore-controlled curve $\sigma^*_{fl}/K_{f,P}$.
5. If the point lies in the interaction band ($K_{f,N} \approx K_{f,P}$): a refined analysis is required, explicitly inserting a representative pore near the hotspot and re-assessing with SED. A conservative lower bound in this band is $\sigma^*_{fl}/(K_{f,N}K_{f,P}) \approx \sigma^*_{fl}/(K_{f,P})^2$.

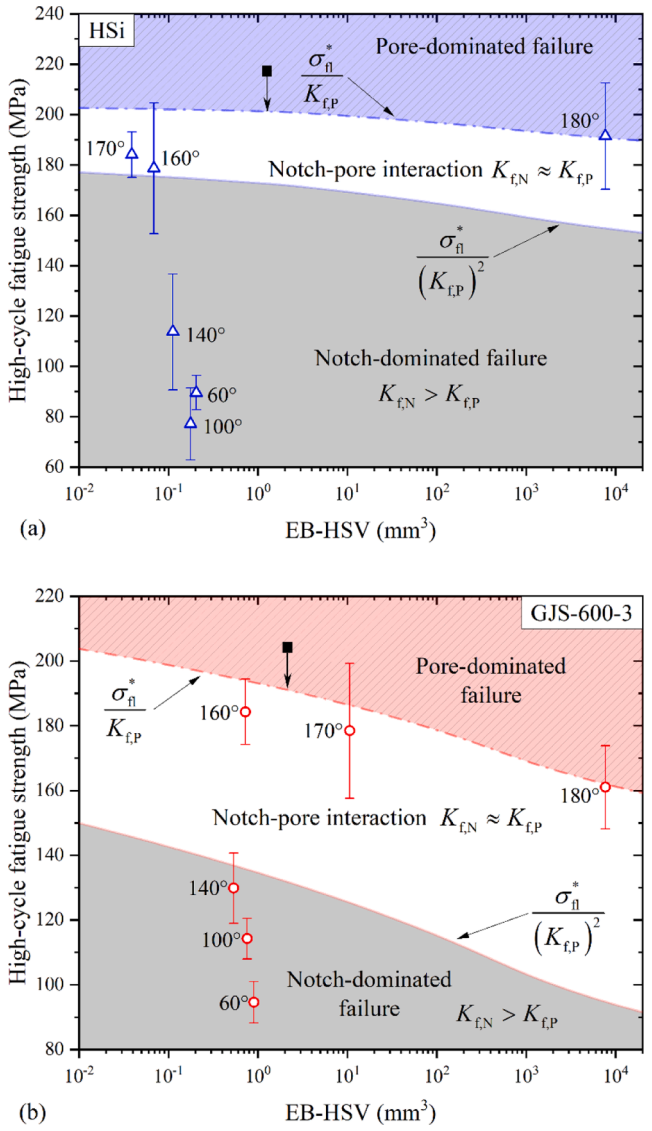

Fig. 13. High-cycle fatigue strength versus EB-HSV (mm^3, log scale) for (a) HSi and (b) GJS-600–3. Symbols: experimental variants annotated by notch opening angle (HSi: triangles; GJS-600–3: circles), plain specimens at 180°. Shaded regions delineate mechanisms based on the relative fatigue stress-concentration factors: notch-dominated when $K_{f,N} > K_{f,P}$ (grey), pore-dominated when $K_{f,P} > K_{f,N}$ (hatched), and a transition band centred on $K_{f,N} \approx K_{f,P}$ (white). A conservative lower bound in the transition assumes full interaction, $\sigma_{fl} \approx \sigma_{fl}^*/(K_{f,N}K_{f,P}) \simeq \sigma_{fl}^*/(K_{f,P})^2$. The filled square illustrates a design "working point" in the pore-dominated regime and the arrow indicates shifting the design strength to the pore-controlled curve $\sigma_{fl}^*/K_{f,P}$.

This workflow enables geometry- and defect-aware design: use notch control when EB-HSV is small, pore control when EB-HSV is large, and perform targeted local modeling in the transition regime.

5. Simplified design and testing guidelines to account for pore-notch competition

The EB-HSV/CT/FE framework in Section 4 is predictive but demanding: it requires CT scans, FE simulations over a pore ensemble to obtain the distribution of $K_{f,P}$, and an iterative evaluation of EB-HSV. In conclusion, we propose a simplified alternative that preserves the key physics and supports day-to-day design without heavy characterization. The analysis on the two nodular cast irons highlights that fatigue damage is governed by different mechanisms in the two extremes:

- Sharp-notch components (small EB-HSV): The probability of hosting a critical shrinkage pore in the relatively small highly stressed volume at the notch root is low. Fatigue is therefore notch-dominated and controlled by the intrinsic behavior of the metallic matrix and its graphite structure.
- Plain or very blunt components (large EB-HSV): The response is pore-dominated: the pore population acts as a family of internal notches and the most critical pore triggers fatigue.

This dichotomy suggests that a small, targeted test matrix is sufficient to calibrate a design-ready model. Specifically, (i) two S–N curves obtained from specimens with sharp notches of different severity (e.g., same opening angle with two root radii, or two opening angles with the same radius) are used to identify the intrinsic fatigue strength of the matrix, σ_{fl}^*, and the SED control radius R_1. In practice, each of the three required fatigue limits—the plain specimen and the two sharp-notched geometries—can be determined from a compact S–N subset consisting of 12 specimens tested at four stress levels with three replicates each. This test layout yielded high-quality Stromeyer fits (Eq. (2), $R^2 \approx 0.99$) and provided σ_{fl}^* estimates with the accuracy needed for the simplified fatigue design workflow.

The notch fatigue stress concentration factor can be obtained from the averaged SED according to Eq. (7). (ii) one S–N curve obtained from tests on plain specimens permits to estimate the plain fatigue strength of the plain specimens (σ_{fl}) weakened by the largest pore expected in its EB-HSV V_{plain}. Given the plain-specimen fatigue limit σ_{fl} and an estimate of the intrinsic fatigue limit σ_{fl}^*, the pore-driven fatigue stress concentration factor associated with the pore family expected in the plain gauge volume V_{plain} is:

$$K_{f,P} = \frac{\sigma_{fl}^*}{\sigma_{fl}} \tag{10}$$

For any notched geometry, compute the notch-driven fatigue factor $K_{f,N}$ (via SED with control radius R_1). As a first-order design check, compare $K_{f,N}$ with $K_{f,P}$ from Eq. (10) to assess whether the geometric notch or the shrinkage-pore population is more critical. The resulting high-cycle fatigue strength σ_{HCF} is then:

$$\sigma_{HCF} = \frac{\sigma_{fl}^*}{K_f}, K_f = \max(K_{f,N}, K_{f,P}) \tag{11}$$

Eq. (11) is qualitatively plotted in the sketch reported in Fig. 14 (solid line). This rule intentionally neglects the mild volume strengthening expected for small EB-HSV (smaller volumes → smaller critical pores), which could be estimated from the pore size distribution using extreme-value statistics. It therefore conservatively uses Eq. (10) for pores so long as the component's EB-HSV does not exceed V_{plain}. Finally, in the transition band where $K_{f,N} \approx K_{f,P}$, notch–pore interaction is expected, as discussed in Section 4 and also demonstrated in [17] by finite element modelling of pores located near the root of the notch. The precautionary lower bound in Fig. 14 (solid red line) accounts for pore–notch interaction by assuming that, in notched components with EB-HSV $< V_{plain}$, a critical pore is present that produces the same $K_{f,P}$ as measured in the plain specimen. Applying the concept sketched in Fig. 14 to the HSi trend in Fig. 10 reveals that the horizontal segment through the plain fatigue limit is very short, reflecting the small gap between σ_{fl}^* and σ_{fl}. In this case, a further simplification is possible: use σ_{fl} directly as an approximation for σ_{fl}^* when determining the control radius R_1—as previously adopted in [35,36]. This expedient is justified by the minimal difference between intrinsic and plain fatigue limits observed for HSi. It will, however, tend to underestimate the fatigue strength for notches with opening angles between 60° and 180° (plain), because it implicitly assumes pore control across that range; this was not an issue in [35,36], where those notch configurations were not investigated.

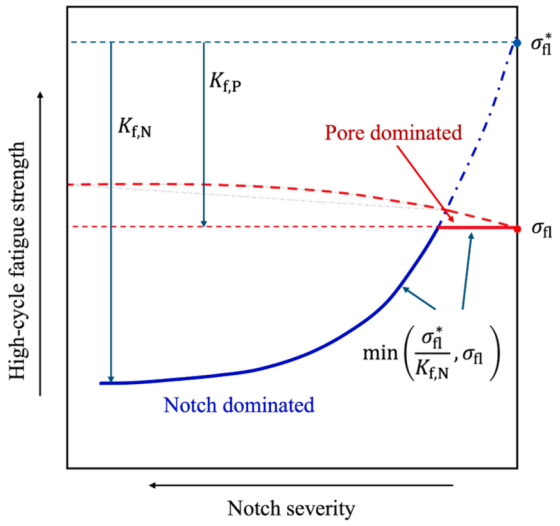

Fig. 14. Simplified design map for predicting high-cycle fatigue strength σ_{HCF} of notched DCI components with shrinkage porosity. The blue solid curve ($\sigma_{fl}^*/K_{f,N}$) represents notch-controlled behavior obtained with the SED approach (control radius R_1). The red dashed curve ($\sigma_{fl}^*/K_{f,P}$, see Fig. 10) represents pore-controlled behavior. This is simplified by the constant trend displayed by the solid red line where the pore factor is estimated from plain tests as $K_{f,P} = \sigma_{fl}^*/\sigma_{fl}$ (Eq. (10). The red solid lower-bound provides a conservative estimate by assuming, for notched components with EB-HSV < V_{plain}, the presence of a pore producing the same $K_{f,P}$ as in the plain specimen. This chart implements a practical alternative to the full EB-HSV/CT/FE framework of Section 4, capturing the two limiting mechanisms: sharp notches (small EB-HSV) → notch-dominated; plain/very blunt geometries (large EB-HSV) → pore-dominated.

In summary, to estimate the fatigue resistance of notched DCI components where shrinkage pores are expected, the workflow in Fig. 15 can be adopted. The procedure delivers a conservative, geometry- and defect-aware prediction while avoiding CT-based characterization and pore-by-pore FE modelling: porosity is treated as an intrinsic defect whose effect is embedded in σ_{fl}, σ_{fl}^*, and $K_{f,P}$. This has immediate practical applicability provided that the adopted plain-specimen geometry samples an EB-HSV comparable to, or larger than, that expected in the component under analysis; otherwise, a volume-effect correction (or an additional plain test with larger gauge volume) should be considered. With these provisions, designers can obtain reliable high-cycle fatigue estimates using minimal testing and analysis effort.

6. Relation to existing defect-sensitive fatigue models

Classical defect-sensitive approaches such as Murakami's $\sqrt{area}$ model [47] and Kitagawa–Takahashi (KT) [48] diagrams describe the fatigue limit as the minimum envelope between an intrinsic fatigue strength and a LEFM-controlled branch governed by the crack-growth threshold ΔK_{th}. In the present work, the intrinsic fatigue limit σ_{fl}^* and the SED control radius R_1 were obtained for each DCI grade by an inversion procedure applied to sharp-notch data, i.e. in a regime where fatigue is governed by the defect-free matrix and graphite structure. Within the TCD/SED framework, σ_{fl}^* and R_1 can be uniquely related to an equivalent ΔK_{th} following Lazzarin and Berto's derivation for mode-I loading [49]. This relationship provides the information needed to recast the present results into a KT-type diagram; the full procedure is detailed in Appendix A. The resulting curves, shown in Fig. 16, reproduce the observed reduction of plain-specimen fatigue strength as the expected pore size increases and correctly bracket the experimentally measured fatigue limits of the two grades. In other words, the intrinsic properties identified through the EB-HSV/SED inversion are fully consistent with a classical KT description of defect-controlled fatigue in plain specimens. This additional comparison supports the soundness of the calibrated σ_{fl}^* and R_1 and indicates that, in the limit of $K_t \to 1$, the present framework reduces to an equivalent KT representation.

It is worth emphasizing that, unlike most defect-sensitive

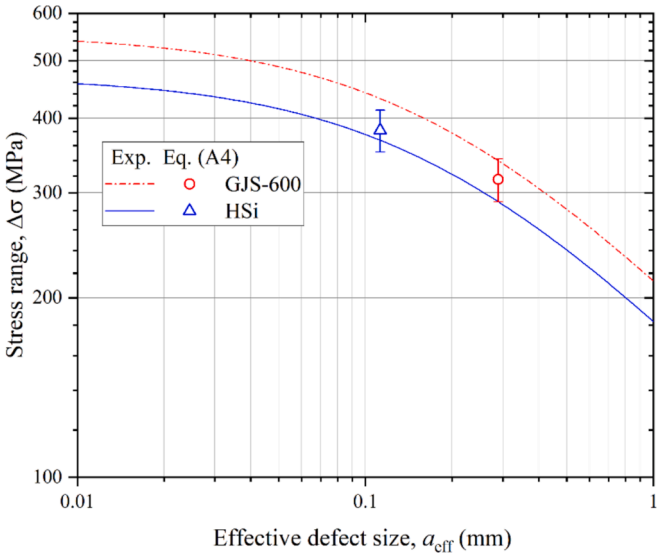

Fig. 16. Kitagawa–Takahashi diagrams for the two DCI grades in terms of effective defect size a_{eff}. Continuous lines: KT curves obtained by combining the intrinsic fatigue limit σ_{fl}^* and the SED control radius R_1 (from the inversion procedure) with the ΔK_{th} estimated according to Lazzarin and Berto's [49], following the methodology elucidated in [50]. Symbols: experimental plain-specimen fatigue limits (with scatter bars) expressed as equivalent a_{eff} values for GJS-600–3 (red circles) and HSi (blue triangles). The KT representation rationalizes the influence of shrinkage pores on the plain fatigue strength and confirms the consistency of the intrinsic parameters identified in this work.

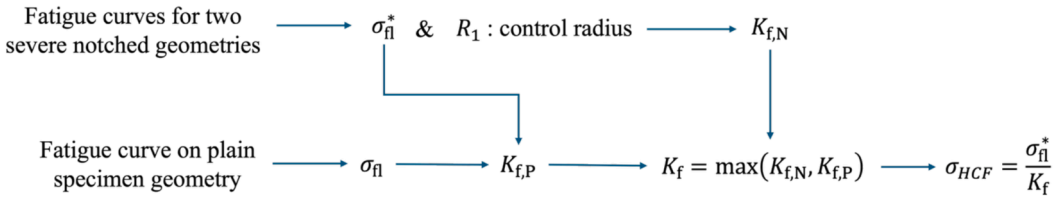

Fig. 15. Workflow for simplified fatigue design of notched DCI components with shrinkage porosity. Inputs from minimal testing: (i) two sharp-notch S–N curves → identify intrinsic fatigue limit σ_{fl}^* and SED control radius R_1; (ii) one plain S–N curve → plain fatigue limit σ_{fl} and pore factor $K_{f,P} = \sigma_{fl}^*/\sigma_{fl}$. Design steps: compute the notch factor $K_{f,N}$ via SED for the target geometry; compare $K_{f,N}$ and $K_{f,P}$; set $K_f = \max(K_{f,N}, K_{f,P})$; predict high-cycle fatigue strength $\sigma_{HCF} = \sigma_{fl}^*/K_f$. If $K_{f,N} \approx K_{f,P}$, use the conservative interaction bound and, if needed, perform a local pore-in-hotspot check. Practical note: the method avoids CT-based characterization and pore-by-pore FE modelling by treating porosity as an intrinsic defect embedded in σ_{fl}, σ_{fl}^*, and $K_{f,P}$. It is applicable provided the plain-specimen EB-HSV is comparable to or larger than that of the component; otherwise, apply a volume-effect correction (or test a larger plain gauge). This yields reliable, conservative estimates with minimal testing and analysis effort.

models—which focus on plain or mildly notched geometries and/or on surface-connected defects [51]—the present approach explicitly treats the competition between a deterministic geometric notch and a stochastic population of internal shrinkage pores in thick-section cast irons. The EB-HSV concept provides the bridge between these two scales: when the EB-HSV is small, the notch-driven SED controls fatigue (notch-dominated regime), whereas for large EB-HSV the response converges to the KT-type defect-controlled behavior summarized in Fig. 16 (pore-dominated regime). In this sense, the proposed methodology can be viewed as an extension of classical KT and TCD/SED concepts to situations where geometry-induced stress concentrations and statistically distributed internal defects act concurrently.

7. Concluding remarks and future work

This work quantified how intrinsic shrinkage pores and geometric notches jointly govern the high-cycle fatigue response of two heavy-section ductile cast irons (DCIs): pearlitic EN-GJS-600–3 and a high-silicon ferritic grade. By combining CT-based defect statistics, strain-energy–density (SED) analysis, and an energy-based highly stressed volume (EB-HSV) definition, we established a predictive framework that separates pore-controlled from notch-controlled initiation and explains the observed behavior across notch severities. The following conclusions can be drawn:

1. GJS-600–3 shows fewer but larger pores and a higher sensitivity to defects; the HSi grade shows many smaller, more irregular pores yet greater defect tolerance.
2. The ranking of fatigue limits reverses as the notch becomes milder (EB-HSV increases): (i) Under sharp notches (small EB-HSV), GJS-600–3 outperforms HSi because intrinsic matrix strength dominates. (ii) For plain or very blunt geometries (large EB-HSV), HSi becomes superior because pore tolerance governs. The switch is gradual, not abrupt—consistent with the larger experimental scatter and fractography showing mixed initiation in the transition band.
3. The framework reproduces the fatigue limits of both plain and notched specimens and correctly identifies the transition region; plain-specimen predictions agree very well with experimental data.
4. By relating the intrinsic fatigue limit and SED control radius to an equivalent ΔK_{th}, a Kitagawa–Takahashi (KT) diagram was constructed for both grades. The resulting KT curves accurately reproduce the experimentally observed influence of shrinkage pores on the plain fatigue strength, confirming that the intrinsic material parameters obtained via EB-HSV/SED inversion are fully consistent with classical defect-sensitive models.
5. Fig. 12 provides a design map that indicates when notch control or pore control is expected. Building on this, we proposed a simplified, test-light rule that uses: (i) two sharp-notch S–N curves to identify the intrinsic fatigue limit and the SED control radius, and (ii) one plain S–N curve to quantify the pore effect. Designers then compare the notch factor from SED with the pore fatigue stress concentration factor from plain tests and size the fatigue limit using the more severe of the two. This delivers a conservative, geometry- and defect-aware estimate without CT surveys or pore-by-pore FE.

This research work suggests the following design implications:

1. Prefer GJS-600–3 for components with sharp stress raisers (small EB-HSV).
2. Prefer HSi for components with blunt features and large EB-HSV, where pore tolerance is decisive.
3. Near the interaction band (notch and pore effects comparable), apply the conservative lower bound from Fig. 14 and, if margins are tight, perform a local check with a representative pore near the hotspot.

The current work is characterized by these limitations:

- The current implementation uses a sharp regime boundary for clarity, whereas the physical transition is stochastic and progressive.
- The simplified rule neglects small-volume strengthening; if a component's EB-HSV is smaller than that of the plain specimen used to calibrate the pore effect, apply a volume correction or test a larger plain gauge.
- The study addresses uniaxial HCF by considering internal micro-shrinkage pores; surface-connected defects, residual stresses, and environmental effects remain outside scope.

Therefore, there is still room for future work:

- Extend the validation to multiaxial and variable-amplitude loading.
- Incorporate the effect of as-cast non-machined surfaces within the same framework.
- Quantify uncertainty in notch and pore factors and propagate to reliability indices or partial safety factors.
- Generalize calibration across additional DCI grades, casting routes, and component scales.
- Explore data-driven surrogates for rapid pore-factor estimation from limited CT descriptors.

Overall, the study delivers both a mechanistic understanding of pore–notch competition and a practical, conservative path to fatigue design of heavy-section DCI components, enabling more informed material–geometry selection with reduced over-conservatism.

CRediT authorship contribution statement

M. Benedetti: Writing – review & editing, Writing – original draft, Supervision, Methodology, Investigation, Funding acquisition, Formal analysis, Conceptualization. **M. Pedranz:** Writing – review & editing, Writing – original draft, Validation, Software, Methodology, Investigation, Formal analysis, Data curation, Conceptualization. **D. Lusuardi:** Writing – review & editing, Supervision, Methodology, Funding acquisition, Conceptualization. **F. Zanini:** Writing – review & editing, Investigation, Data curation. **S. Carmignato:** Writing – review & editing, Investigation, Formal analysis, Data curation. **V. Fontanari:** Writing – review & editing, Writing – original draft, Validation, Supervision, Methodology, Funding acquisition, Conceptualization.

Declaration of competing interest

The authors declare the following financial interests/personal relationships which may be considered as potential competing interests: Matteo Pedranz reports financial support was provided by CNR - National Research Council. Matteo Pedranz reports financial support was provided by Fonderie Ariotti Spa. If there are other authors, they declare that they have no known competing financial interests or personal relationships that could have appeared to influence the work reported in this paper.

Acknowledgments

The present study received funding from Consiglio Nazionale delle Ricerche (CNR), Italy and Fonderie Ariotti SpA in the form of a PhD grant for author Matteo Pedranz (doctorate school of Innovazione Industriale at the University of Trento).

Appendix A

To quantify the influence of micro-shrinkage pores on the high-cycle fatigue strength of the plain specimens, a fracture mechanics approach based on the Kitagawa–Takahashi (KT) diagram [48] was adopted. In this framework, defects are modelled as cracks of effective size [52]

$$a_{eff} = Y^2 \bullet \sqrt{area} \tag{A1}$$

where Y is the defect shape factor (0.5 for internal defects and 0.65 for surface-breaking defects), and $\sqrt{\text{area}}$ is Murakami's defect parameter [47], representing the square root of the projected defect area on a plane perpendicular to the loading axis.

The long-crack threshold stress-intensity-factor range ΔK_{th} was evaluated following the approach proposed by Lazzarin and Berto [49]. Under plane-strain conditions, ΔK_{th} is derived from the intrinsic plain-fatigue-limit range $\Delta\sigma_{fl}^{*} = 2\sigma_{fl}^{*}$ and the control radius R_1:

$$\Delta K_{th} = \Delta\sigma_{fl}^{*} \bullet \sqrt{\frac{4\pi}{(5-8\nu) \bullet (1+\nu)} R_1} \tag{A2}$$

where v is the Poisson' ratio (v=0.27 in the present case). Using this value, the El Haddad–Smith–Topper intrinsic crack length parameter [53] can be determined as:

$$a_0 = \frac{1}{\pi}\left(\frac{\Delta K_{th}}{\Delta\sigma_{fl}^{*}}\right)^2 \tag{A3}$$

For a defect treated as a crack of effective size a_{eff}, the threshold stress range for non-propagation is then given by [50,52]:

$$\Delta\sigma_{th} = \frac{\Delta K_{th}}{\sqrt{\pi\left(a_{eff} + a_0\right)}} \tag{A4}$$

Equation (A4) is represented in the KT diagram shown in Fig. 16, where the values of the relevant quantities are listed in Table A1 for both cast iron grades. Fig. 16 also reports the experimental high-cycle fatigue strengths of the plain specimens. The effective crack sizes a_{eff} were obtained from a statistical analysis of the internal-defect population ($Y = 0.5$) detected in the plain specimens by CT scanning, using the 99 % cumulative probability as reference.

Table A1
Material and defect characteristics used to build the KT diagram shown in Fig. 16.

Cast iron	ΔK_{th} (MPa$\sqrt{\text{m}}$)	a_0 (mm)	a_{eff} (mm)
GJS600	13.0	0.174	0.289
HSi	11.1	0.177	0.113

Data availability

Data will be made available on request.

References

[1] Stefański Z, Kamińska J, Pamuła E, Angrecki M, Palma A. Comparing the effectiveness of cast iron spheroidization by the traditional method and using a reaction chamber (reactor) placed in foundry mould. Archieves of Foundry Engineering 2018;18:191–5.
[2] *Complete Casting Handbook*. Elsevier, 2015. doi: 10.1016/C2014-0-01548-1.
[3] Asi O. Failure analysis of a crankshaft made from ductile cast iron. Eng Fail Anal 2006;13(8):1260–7. https://doi.org/10.1016/j.engfailanal.2005.11.005.
[4] Akinribide OJ, et al. A review on heat treatment of cast iron: phase evolution and mechanical characterization. Materials 2022;15(20):7109. https://doi.org/10.3390/ma15207109.
[5] Tanabi H, Rafighi M. Turning machinability of alloyed ductile iron compared to forged EN 1.7131 steel. Mater Test 2020;62(12):1259–64. https://doi.org/10.3139/120.111612.
[6] Borsato T, Ferro P, Berto F, Carollo C. Effect of solidification time on microstructural, mechanical and fatigue properties of solution strengthened ferritic ductile iron. Metals (Basel) 2018;9(1):24. https://doi.org/10.3390/met9010024.
[7] Foglio E, Lusuardi D, Pola A, La Vecchia GM, Gelfi M. Fatigue design of heavy section ductile irons: influence of chunky graphite. Mater Des 2016;111:353–61. https://doi.org/10.1016/j.matdes.2016.09.002.
[8] Hütter G, Zybell L, Kuna M. Micromechanisms of fracture in nodular cast iron: from experimental findings towards modeling strategies – a review. Eng Fract Mech 2015;144:118–41. https://doi.org/10.1016/j.engfracmech.2015.06.042.
[9] D. M. Stefanescu, *Science and Engineering of Casting Solidification*. Cham: Springer International Publishing, 2015. doi: 10.1007/978-3-319-15693-4.
[10] Ohnaka I, Iwane J, Yasuda H, Zhu J. Prediction of porosity defect in spheroidal graphite iron castings. Int J Cast Met Res 2003;16(1–3):293–9. https://doi.org/10.1080/13640461.2003.11819598.
[11] Regordosa A, Llorca-Isern N. Microscopic characterization of different shrinkage defects in ductile irons and their relation with composition and inoculation process. Int J Met 2017;11(4):778–89. https://doi.org/10.1007/s40962-016-0120-9.
[12] Khalajzadeh V, Beckermann C. Simulation of shrinkage porosity formation during alloy solidification. Metall Mater Trans A 2020;51(5):2239–54. https://doi.org/10.1007/s11661-020-05699-z.
[13] Stefanescu DM. Computer simulation of shrinkage related defects in metal castings – a review. Int J Cast Met Res 2005;18(3):129–43. https://doi.org/10.1179/136404605225023018.
[14] Ghassemali E, Jarfors A, Diószegi A. On the formation of micro-shrinkage porosities in ductile iron cast components. Metals (Basel) 2018;8(7):551. https://doi.org/10.3390/met8070551.
[15] Borsato T, Berto F, Ferro P, Carollo C. Influence of solidification defects on the fatigue behaviour of heavy-section silicon solution–strengthened ferritic ductile cast irons. Fatigue Fract Eng Mater Struct 2018;41(11):2231–8. https://doi.org/10.1111/ffe.12810.
[16] Nadot Y. Influence of casting defects on the fatigue limit of nodular cast iron. Int J Fatigue 2004;26(3):311–9. https://doi.org/10.1016/S0142-1123(03)00141-5.
[17] Pedranz M, et al. A new energy based highly stressed volume concept to investigate the notch-pores interaction in thick-walled ductile cast iron subjected to uniaxial fatigue. Int J Fatigue 2023;169:107491. https://doi.org/10.1016/j.ijfatigue.2022.107491.
[18] Rennert R, Vormwald M, Esderts A. FKM-guideline 'Analytical strength Assessment' – Background and current developments. Int J Fatigue 2024;182:108165. https://doi.org/10.1016/j.ijfatigue.2024.108165.

[19] Takemoto Y, Mizumoto M, Kinno K. Internal porosity defects in ductile cast irons. Int J Met 2021;15(3):916–29. https://doi.org/10.1007/s40962-020-00527-x.
[20] B. Ravi, *Metal Casting: Computer Aided Design and Analysis*. Prentice-Hall of India Pvt.Ltd, 2011.
[21] Niyama E, Uchida T, Morikawa M, Saito S. Predicting shrinkage in large steel castings from temperature gradient calculations. Int J Cast Met Res 1981;6(2):16–22.
[22] Ignaszak Z. Discussion on usability of the niyama criterion for porosity predicting in cast iron castings. Arch Foundry Eng 2017;17(3):196–204. https://doi.org/10.1515/afe-2017-0115.
[23] S. Bin Kim, Y. H. Yim, J. M. Yoon, and D. M. Ştefănescu, "Prediction of Shrinkage Defects in Iron Castings Using a Microporosity Model," *Materials Science Forum*, vol. 925, pp. 411–418, Jun. 2018, doi: 10.4028/www.scientific.net/MSF.925.411.
[24] J. Devlukia, G. Bargmann, and I. Rüstenberg, "Fatigue Assessment of an Automotive Suspension Component using Deterministic and Probabilistic Approaches," 1997, pp. 1–16. doi: 10.1016/S1566-1369(97)80003-9.
[25] Murakami Y, Usuki H. Quantitative evaluation of effects of non-metallic inclusions on fatigue strength of high strength steels. II: Fatigue limit evaluation based on statistics for extreme values of inclusion size. Int J Fatigue 1989;11(5):299–307. https://doi.org/10.1016/0142-1123(89)90055-8.
[26] Murakami Y. Inclusion rating by statistics of extreme values and its application to fatigue strength prediction and quality control of materials. J Res Nat Inst Stand Technol 1994;99(4):345. https://doi.org/10.6028/jres.099.032.
[27] Wang R, Li D, Hu D, Meng F, Liu H, Ma Q. A combined critical distance and highly-stressed-volume model to evaluate the statistical size effect of the stress concentrator on low cycle fatigue of TA19 plate. Int J Fatigue 2017;95:8–17. https://doi.org/10.1016/j.ijfatigue.2016.10.003.
[28] Hertel O, Vormwald M. Statistical and geometrical size effects in notched members based on weakest-link and short-crack modelling. Eng Fract Mech 2012;95:72–83. https://doi.org/10.1016/j.engfracmech.2011.10.017.
[29] Kloos KH, Buch A, Zankov D. Pure Geometrical size effect in fatigue tests with constant stress amplitude and in programme tests. Materwiss Werksttech 1981;12(2):40–50. https://doi.org/10.1002/mawe.19810120205.
[30] Z. P. Bažant, "Size effect on structural strength: a review," *Archive of Applied Mechanics (Ingenieur Archiv)*, vol. 69, no. 9–10, pp. 703–725, Nov. 1999, doi: 10.1007/s004190050252.
[31] El Khoukhi D, Morel F, Saintier N, Bellett D, Osmond P, Le V-D. Probabilistic modeling of the size effect and scatter in high cycle fatigue using a monte-carlo approach: role of the defect population in cast aluminum alloys. Int J Fatigue 2021;147:106177. https://doi.org/10.1016/j.ijfatigue.2021.106177.
[32] Ai Y, Zhu S-P, Liao D, Correia JAFO, De Jesus AMP, Keshtegar B. Probabilistic modelling of notch fatigue and size effect of components using highly stressed volume approach. Int J Fatigue 2019;127:110–9. https://doi.org/10.1016/j.ijfatigue.2019.06.002.
[33] D. Taylor, "Introduction," in *The Theory of Critical Distances*, Elsevier, 2007, pp. 1–19. doi: 10.1016/B978-008044478-9/50002-8.
[34] Berto F, Lazzarin P. A review of the volume-based strain energy density approach applied to V-notches and welded structures. Theor Appl Fract Mech 2009;52(3):183–94. https://doi.org/10.1016/j.tafmec.2009.10.001.
[35] Pedranz M, Fontanari V, De Biasi R, Berto F, Santus C, Benedetti M. A simplified strain energy density approach for multiaxial fatigue predictions. Int J Mech Sci 2025;288:109961. https://doi.org/10.1016/j.ijmecsci.2025.109961.
[36] Pedranz M, Fontanari V, Santus C, Lusuardi D, Berto F, Benedetti M. A strain energy density design approach for large cast iron components: from microstructural analysis to multiaxial fatigue response. Int J Fatigue 2023;175:107824. https://doi.org/10.1016/j.ijfatigue.2023.107824.
[37] Pelizzari J, Campagnolo A, Dengo C, Meneghetti G. A master curve for fatigue design of notched nodular cast iron components based on the local averaged strain energy density. Materials 2024;17(19):4807. https://doi.org/10.3390/ma17194807.
[38] Vaara J, Väntänen M, Laine J, Kemppainen J, Frondelius T. Prediction of the fatigue limit defining mechanism of nodular cast iron based on statistical microstructural features. Eng Fract Mech 2023;277:109004. https://doi.org/10.1016/j.engfracmech.2022.109004.
[39] Ikeda T, Umetani T, Kai N, Noda N-A, Sano Y. Strain rate and temperature insensitiveness of notch-bend strength for high Si ductile cast iron. ISIJ Int 2016;56(5):868–74. https://doi.org/10.2355/isijinternational.ISIJINT-2015-516.
[40] Ebel A, Marsan O, Lacaze J, Malard B. Cyclic oxidation of high-silicon spheroidal graphite iron. Corros Sci 2021;192:109854. https://doi.org/10.1016/j.corsci.2021.109854.
[41] Beretta S, Murakami Y. Statistical analysis of defects for fatigue strength prediction and quality control of materials. Fatigue Fract Eng Mater Struct 1998;21(9):Sep. https://doi.org/10.1046/j.1460-2695.1998.00104.x.
[42] *Betriebsfestigkeit*. Berlin/Heidelberg: Springer-Verlag, 2006. doi: 10.1007/3-540-29364-7.
[43] Benedetti M, Santus C, Fontanari V, Lusuardi D, Zanini F, Carmignato S. Plain and notch fatigue strength of thick-walled ductile cast iron EN-GJS-600-3: a double-notch critical distance approach to defect sensitivity. Int J Fatigue 2021;152:106414. https://doi.org/10.1016/j.ijfatigue.2021.106414.
[44] Makkonen L, Rabb R, Tikanmäki M. Size effect in fatigue based on the extreme value distribution of defects. Mater Sci Eng A 2014;594:68–71. https://doi.org/10.1016/j.msea.2013.11.045.
[45] He J-C, et al. Microstructural size effect on the notch fatigue behavior of a Ni-based superalloy using crystal plasticity modelling approach. Int J Plast 2024;172:103857. https://doi.org/10.1016/j.ijplas.2023.103857.
[46] Berto F, Ferro P, Salavati H. Fatigue strength of sharp V-notched specimens made of ductile cast iron. Eng Fail Anal 2017;82:308–14. https://doi.org/10.1016/j.engfailanal.2017.04.001.
[47] Murakami Y, Endo M. Effects of defects, inclusions and inhomogeneities on fatigue strength. Int J Fatigue 1994;16(3):163–82. https://doi.org/10.1016/0142-1123(94)90001-9.
[48] Kitagawa H and Takahashi S, "Applicability of fracture mechanics to very small cracks or the cracks in the early stage," in *Proceedings of Second International Conference on Mechanical Behavior of Materials*, 1976, pp. 627–631.
[49] Lazzarin P, Berto F. From Neuber's Elementary volume to Kitagawa and Atzori's diagrams: an interpretation based on local energy. Int J Fract 2005;135(1–4):L33–8. https://doi.org/10.1007/s10704-005-4393-x.
[50] Benedetti M, Santus C. Building the Kitagawa-Takahashi diagram of flawed materials and components using an optimized V-notched cylindrical specimen. Eng Fract Mech 2020;224:106810. https://doi.org/10.1016/j.engfracmech.2019.106810.
[51] Collini F, Meneghetti G. Towards a fracture mechanics-based fatigue assessment of lattice structures obtained from additive manufacturing of metallic powders. Mater Des 2024;244:113077. https://doi.org/10.1016/j.matdes.2024.113077.
[52] Meneghetti G, Rigon D, Gennari C. An analysis of defects influence on axial fatigue strength of maraging steel specimens produced by additive manufacturing. Int J Fatigue 2019;118:54–64. https://doi.org/10.1016/j.ijfatigue.2018.08.034.
[53] El Haddad MH, Topper TH, Smith KN. Prediction of non propagating cracks. Eng Fract Mech 1979;11(3):573–84. https://doi.org/10.1016/0013-7944(79)90081-X.